Pure Appl. Chem., Vol. 77, No. 8, pp. 1395–1408, 2005.
DOI: 10.1351/pac200577081395

Control of spiral instabilities in reaction–diffusion systems*

Hui-Min Liao[1], Min-Xi Jiang[1], Xiao-Nan Wang[1], Lu-Qun Zhou[1], and Qi Ouyang[1,2,‡]

[1]Department of Physics; [2]Center for Theoretical Biology, Peking University, Beijing 100871, P.R. China

Abstract: Spiral instabilities and their controls are investigated in a reaction–diffusion system using the Belousov–Zhabotinsky reaction. Two spiral instabilities, the long-wavelength instability and the Doppler instability, are reported, which can lead to spatiotemporal chaos. The long-wavelength instability occurs in an oscillatory regime, while the Doppler instability occurs in an excitable regime. To control these two instabilities, two different strategies are proposed according to their defect-generating mechanisms. For the long-wavelength instability in an oscillatory system, the control can be achieved by introducing a local pacemaker, which emits stable traveling waves to sweep off the unstable spiral defects. For the Doppler instability, the control can be achieved by trapping the spiral tip with a local area of higher diffusion coefficient than its surroundings.

Keywords: Spiral instabilities; Belousov–Zhabotinsky reaction; long-wavelength instability; Doppler instability; reaction–diffusion.

INTRODUCTION

In reaction–diffusion systems, a spiral wave is one of the characteristic patterns that widely exist in chemical, biological, physiological, and physical systems. A normal spiral consists of a spiral tip and traveling waves; the tip rotates around a regular circle, sending the waves out. In a certain range of control parameters, the normal spiral may lose its stability: it may meander, with its tip giving cycloid trajectory, or even break, with more and more new tips generated, making the whole system chaotic. Transitions from ordered spiral waves to defect-mediated turbulence have been well studied in theory [1–5], and observed both in experiments [6–9] and numerical simulations [10–13]. The study of transitions to defect-mediated turbulence becomes one of the most promising routes to investigate spatiotemporal chaos. Moreover, studies on animal hearts show that the motion of spiral waves is closely related to re-entrant excitation, and the instability of the spiral waves leads to cardiac fibrillation, which causes life-threatening situations [14–16]. So understanding spiral dynamics and control spiral instabilities are of great value both in theory and application.

Spiral waves in reaction–diffusion systems can be sorted into two categories: spirals in excitable systems and spirals in oscillatory systems. The dynamical behavior of spiral waves in an excitable medium is governed by the dispersion relation, which relates the speed to the period of traveling waves,

*Paper based on a presentation at the 18th IUPAC International Conference on Chemical Thermodynamics (ICCT-2004), 17–21 August 2004, Beijing, China. Other presentations are published in this issue, pp. 1297–1444.

‡Corresponding author

and the critical relation, which relates the rotating speed to the wave front curvature [17]. In the dispersion relation, there exists a minimum period, below which the system cannot recover to its excitable state, and traveling waves cease to exist [17,18]. When the Doppler instability occurs, owing to the Doppler effect, the local period of spiral waves becomes less than the minimum period, rendering the local chemical waves unstable; thus, defects are spontaneously created. In this case, the key of effective control of spiral instability is to confine the motion of the spiral tip. In previous studies, researchers have successfully controlled an excitable spiral tip with external influences [19] and localized inhomogeneities of defects [20]. We find that the local difference of diffusion coefficient can also lead to the attraction of the spiral tip [21]. It may afford us a new way to control the instability caused by meandering of the spiral tip.

Spirals in oscillatory systems are generated with the spatiotemporal phase difference of the periodic oscillations. When the reaction–diffusion system is near a supercritical Hopf bifurcation, it can be described by the complex Ginzburg–Landau equation (CGLE). Wave instabilities have been extensively studied in the CGLE [22]. In our Belousov–Zhabotinsky (BZ) reaction system, the long-wavelength instability, under which the spiral is modulated by a long-wavelength wave and the modulation has a convective nature, is possibly related to Eckhaus instability in CGLE systems. In a CGLE system, people have achieved the spatiotemporal turbulence control through tracing and stabilizing one previously unstable wave-generating defect by injecting weak perturbations near the defect core [23,24]. Thus, a stable spiral is developed to cover the entire uncontrolled region along the wave propagation direction. Recently, we find that by introducing a local pacemaker at a random location in the system described by a two-dimensional (2D) CGLE, spiral turbulence can be controlled by a stable target wave produced around the pacemaker [25]. We hope this simple and effective method can be applied in reaction–diffusion systems.

In this paper, we review our systematic experimental studies of dynamical behaviors of spiral waves and spiral instabilities in a spatially extended BZ reaction system. Then, according to the analysis of the mechanisms leading to chemical turbulence in the two instabilities, we discuss two new strategies to control the two instabilities, respectively.

EXPERIMENTAL SET-UP

Our experiments are conducted in a spatial open reactor [26], using the ferroin [$Fe(phen)_3^{2+}$] catalyzed BZ reaction. The heart of the reactor is a thin porous glass disk (Vycor glass, Corning), 0.4 mm thick and 19 mm in diameter, which has 25 % void space and 100 Å average pore size. The porous glass is used to prevent convection in the reaction medium. Each surface of the disk is in contact with a compartment where the reactant concentrations are kept homogeneous and constant by highly precise pumps and magnetic stirrers. The chemicals are fed asymmetrically: malonic acid and potassium bromide are fed on side A, sulfuric acid and ferroin are fed on side B, sodium bromate is fed on both sides, so that side A is kept fixed in a reduced state and side B in an oxidized state. Both sides are kept from oscillating. The chemicals diffuse into the porous glass, where the BZ reaction occurs and patterns form. Because multiple chemical gradients exist across the reaction medium, our system is in fact quasi-2D. However, previous studies [27,28] show that if the boundary conditions are uniform, under certain conditions, the quasi-2D system with gradients in the third dimension (like our experimental set-up) behaves qualitatively like a 2D system.

In the experiments, we use a helium–neon laser (10 mW, $\lambda = 633$ nm) to generate and guide spirals [29]. The beam from the laser is used to break a chemical wave into a pair of spiral rotors, then one of the spiral rotors is guided to the edge of reaction medium; at last, it is absorbed and disappears. Thus, initial conditions can be chosen such that only one spiral resides in the middle of the system. Once a spiral is prepared, we study it by increasing or decreasing one chemical concentration in a stepwise fashion while fixing the others. Enough time is allowed between changes so that the system can relax to its new asymptotic state. The typical waiting time is about 1 h. The reactor is illuminated by a blue

light source (about 550 nm). Images of the patterns are taken by a charge-coupled device camera, then digitized and stored in a computer for later processing.

Previous studies [30] show that the dynamics of spiral waves is most sensitive to three control parameters: the concentrations of sulfuric acid ($[H_2SO_4]$), malonic acid ([MA]) and sodium bromate ($[NaBrO_3]$). We choose $[H_2SO_4]$ and [MA] as control parameters. Other reactant concentrations of the BZ reaction are kept fixed. The experimental temperature is 25 ± 0.5 °C.

PHASE DIAGRAM

Figure 1 gives a slice of the phase diagram using [MA] and $[H_2SO_4]$ as control parameters, with $[NaBrO_3]$ is fixed at 0.6 M, [KBr] = 0.03 M, [ferroin] = 1.5 mM. About 80 different points are studied and categorized. The phase diagram can be divided into several domains, each is labeled according to the observed patterns: simply rotating spiral (S), meandering spiral (M), chemical turbulence due to the Doppler instability (D), convectively unstable spiral (C), and chemical turbulence due to the long wavelength instability (T). The solid lines indicate the onsets of different instabilities of spirals. The dashed lines are the extrapolation of the solid lines. In regions M and D, the medium is excitable, where the wave front is very sharp. In the region S near the S–C boundary, the medium is oscillatory, where the waves far from the sources can be well described with sinusoidal oscillations.

The S–M boundary in the phase diagram defines a transition from simple spirals to meandering spirals. At the onset, the trajectory of the spiral tip undergoes a Hopf bifurcation [29]. As a result, it changes from a simple circle to an epicycloid or a hypocycloid, and the local behavior of the spiral waves changes from periodic to quasi-periodic. In the meandering state, owing to the Doppler effect, the tip of a spiral emits waves that are compressed in front of the tip and dilated behind the tip. Thus, the local wavelength of spiral waves is no longer constant but changes periodically between a maximum and a minimum value. The ensemble of local maximum wavelength forms a super-spiral. If one continues to decrease [MA] or to increase $[H_2SO_4]$ to cross the M–D boundary (see Fig. 1), the Doppler instability will take place and defects are perpetually generated near the spiral heads, until chemical turbulence occupies the whole reaction medium.

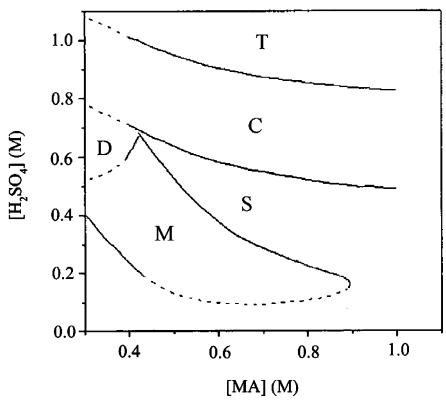

Fig. 1 The phase diagram studied in our experiments with [MA] and $[H_2SO_4]$ as the control parameters. The solid lines indicate the onsets of different instabilities. The dashed lines are the extrapolation of the solid lines.

The C regimes in the phase diagram represent regions where spiral waves undergo a long-wavelength instability that has a convective nature. Before the onset, one observes a stable simple rotating spiral. At the onset of the instability (S–C boundary in Fig. 1), a long-wavelength modulated spiral appears upon the carrier waves. This modulation spiral seems stable within our finite size of reaction medium. Beyond the onset, defects can be generated far away from the spiral center. However, owing

to the convective nature of the instability [31], stable modulated waves can exist in a finite size, surrounded by a defect sea. With the increase of $[H_2SO_4]$, the region of defect-mediated turbulence continuously invades the region of stable modulated waves, until the latter fully disappears as the control parameter crosses the C–T boundary in the phase diagram. As a result, the chemical turbulence in the whole reaction medium forms.

LONG-WAVELENGTH INSTABILITY

When the long-wavelength instability takes place, sustained long-wavelength modulated spiral waves will appear, but the pattern is stable in the finite size of the reactor. As the amplitude of modulation increases with control parameters, spiral waves break. Defects are generated far away from the center, as a result of the neighboring two wave fronts being too close.

We choose the sulfuric acid concentration in reservoir B as the control parameter, keeping the other parameters fixed as described in the capture of Fig. 2. When the concentration of the sulfuric acid is below 0.72 M, one observes a normal spiral. Figure 2a gives an example of such a state, where the gray level of the picture corresponds to the concentration of ferroin. As the control parameter is increased to across a critical value (0.72 M), the long-wavelength instability settles in. Apparent spatially modulated waves emerge so that the distance between successive wave fronts (the local wavelength) varies spatially, as shown in Figs. 2b and 2c. The optical intensity I(x) of the spiral waves along the distance from the spiral core is shown in Fig. 3a. It has clear amplitude and phase modulations. Figure 3b shows the local wavelength variation, which is obtained by wavelet technique. One observes that the phase modulation is spatially periodic, and it goes in phase with amplitude modulation. This is consistent with the observation in ref. [31]. The spatial Fourier spectrum, as shown in Fig. 3c, exhibits two independent peaks at k_c and k_m, corresponding, respectively, to the carrier and the modulation wave number. The ratio of the two wave numbers is 5.33, thus, the instability is of a long-wavelength type. Between $[H_2SO_4]_B$ = 0.72, 0.94 M, no additional defects appear and the long-wavelength-modulated

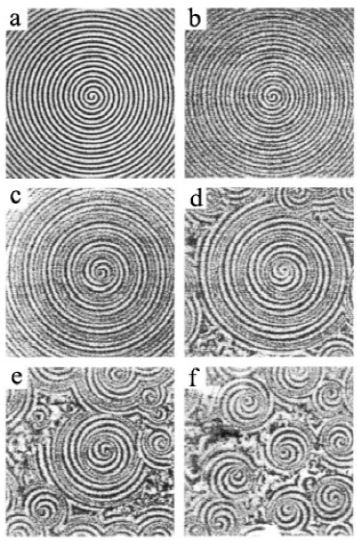

Fig. 2 The snapshots of long-wavelength-modulated spirals and defect-mediated turbulence. $[H_2SO_4]_B$ (in M): (a) 0.63, simple periodic spiral; (b) 0.765, onset of the long-wavelength instability; (c) 0.90, fully developed modulated spirals; (d) 0.94 and (e) 0.95, onset and beyond of defect-mediated turbulence; (f) 0.97, a state of compact laminar disks. Other control parameters are kept fixed: $[MA]_A$ = 0.4 M, $[KBr]_B$ = 30 mM, $[NaBrO_3]_{A(B)}$ = 0.6 M, $[ferroin]_B$ = 1.0 mM, and temperature 25 ± 0.5 °C. The images shown are 13.3 × 13.3 mm.

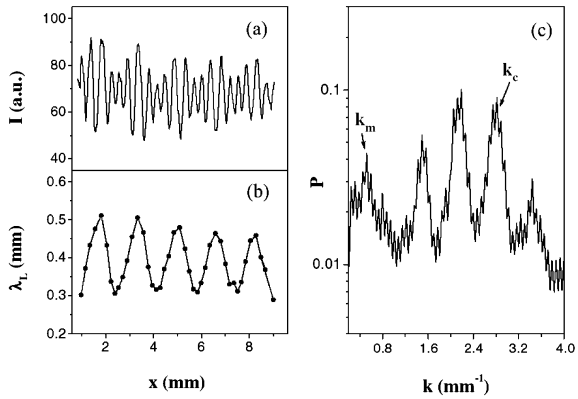

Fig. 3 Measurements of the long-wavelength instability in Fig. 2c. (a) Optical intensity of spiral waves as a function of the distance from the spiral core. (b) The variation of local wavelength with the distance. (c) The spatial power spectrum.

spiral is sustained in the finite reaction medium. If we follow one wave front for the long-wavelength instability, the local wavelength varies, which means that the modulation waves have a relative velocity (named convective velocity) V_g to the carrier waves. In our experiments, the direction of the convective velocity points to the center of the spiral waves. The convective velocities become larger with the increase of control parameter. From these results, the onset of the long-wavelength instability is possibly due to the Eckhaus instability, which we describe in the next section.

As the control parameter is increased across another threshold (0.94 M), defects are continuously generated, see Figs. 2d–2f. The spiral breakup takes place far away from the center, and there exists a disk of laminar core of the spiral where turbulence cannot invade. Thus, the system is separated into two different regimes: ordered spiral waves inside the core and defect-mediated turbulence outside the core. The size of laminar core decreases as the control parameter increases. However, in the turbulence some of the defects have chances to develop into spirals, generating many laminar cores of ordered spirals. The sizes of the laminar cores tend to be equal, and the cores tend to form a compact pattern, see Fig. 2f. At last, when $[H_2SO_4]$ is above 1.0 M, the turbulence state will invade the whole space, which is not shown here.

CONTROL OF LONG-WAVELENGTH INSTABILITY

In an oscillatory system near the onset of Hopf bifurcation, the system's variable can be written as a function of time *t*:

$$u \approx u_0 + A\left(R,T\right)\exp\left(i\omega_{\mathrm{H}}T\right) + c.c. \tag{1}$$

In the ferroin-catalyzed BZ reaction, u corresponds to the concentration of ferroin, ω_H is the Hopf frequency, and A is the complex amplitude of oscillations. The dynamics that A obeys can be simplified to a CGLE. It has the form

$$\frac{\partial A}{\partial t} = A - \left(1+ic\right)\left|A\right|^2 A + \left(1+ib\right)\nabla^2 A \tag{2}$$

where b, c are real control parameters, $\nabla^2 = \partial^2/\partial x^2 + \partial^2/\partial y^2$, and $A(\mathbf{r},t)$ is the complex variable. A steadily rotating spiral solution of eq. 2 has the general form

$$A\left(\mathbf{r},t\right) = F\left(\mathbf{r}\right)\exp\left\{i\left[\sigma\theta + \psi\left(\mathbf{r}\right) - \omega t\right]\right\} \tag{3}$$

For large r, the spiral wave asymptotes to a plane wave with the wave number $k = (d\psi/dr)|_{r\to\infty}$, which is independent of r. Substituting the constant amplitude plane wave solution $A = \sqrt{1-k^2}\exp(ikr - i\omega t)$ into eq. 2, one can get the following dispersion relation:

$$\omega = c + (b - c)k^2 \tag{4}$$

If one ignores the curvature effect, a target wave solution can be considered as a plane wave solution, so that the dispersion relation of eq. 4 is approximately valid to target wave solutions.

The linear stability analyses [32,33] show that in the long wavelength limit, the complex growth rate λ as a function of the wave number of inhomogeneous perturbations p satisfies:

$$\lambda(p) = iv_g p - D_{//}p^2 + O(p^3)$$

where $v_g = 2(c - b)k$ and $D_{//} = 1 + bc - 2k^2(1 + c^2)/(1 - k^2)$. When $D_{//} < 0$, the so-called Eckhaus instability occurs. This instability is a long-wavelength instability and has convective nature. When $1 + bc < 0$, the so-called Benjamin–Feir instability occurs, and the system is unstable for all planar waves with any wave number k, as $D_{//} < 0$.

A cut of the phase diagram in the b-c-k parameter space with fixed $b = -1.4$ is shown in Fig. 4. Several regions where the plane-wave solution has different stabilities [22] are shown. The convectively unstable region is due to Eckhaus instability, where the traveling waves of certain wave numbers can remain stable in the convective sense, because the growth rate of a perturbation is smaller than the traveling speed of the waves. In the absolutely unstable region, the perturbation growth rate becomes larger than the wave speed. In this case, the system will quickly fall into a state of defect-mediated turbulence. For a spiral wave solution, the wave number k is uniquely determined by the parameters b and c, as shown in Fig. 4. Thus, with a fixed value $b = -1.4$, there exists a critical value $c_0 = 0.8$, beyond which the system undergoes the transition from ordered spiral waves to spiral turbulence.

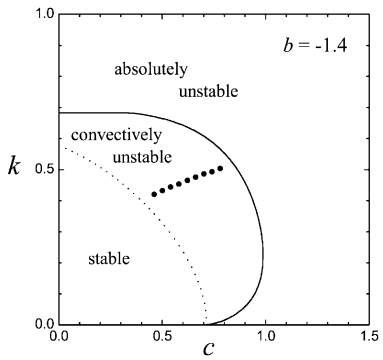

Fig. 4 Regions with different stabilities in the k-c plane with $b = -1.4$. The solid line and dotted line are the onset of absolute instability and convective instability, respectively. The wave numbers of the spiral waves (dark dots) are uniquely decided by the parameters b and c.

Under the assumption that the spiral waves described in the previous section are due to a Hopf bifurcation, and that the instability described in the previous section is due to Eckhaus instability, we develop our spiral instability control strategy. Our study focuses on controlling spiral turbulence in the absolutely unstable region. In the following numerical simulations, the space variables are discretized to 256×256 sites under no-flux boundary conditions. We start with random initial conditions with parameter $c = 0.9$, which is in the absolutely unstable region, as shown in Fig. 4. We wait until the state of spiral turbulence is fully developed; an example of such a state is shown in Fig. 5a. Then, at control

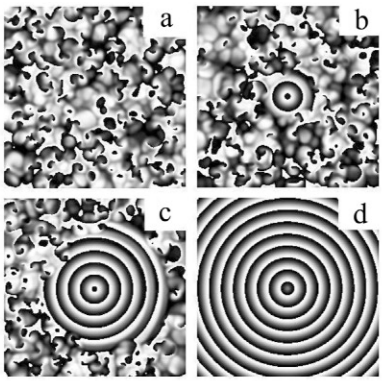

Fig. 5 Numerical simulation of the spiral turbulence control with a target wave. (a) $t = 0$, the control starts; (b) $t =$ 450 t.u., the target wave appears; (c) $t = 1000$ t.u., the target wave almost dominates the system; (d) $t = 1500$ t.u., the whole system is occupied by a large target wave.

time $t = 0$, we introduce to the system a spatially localized pacemaker by changing parameter c from 0.9 to $c_I = 0.6$ in the central 5×5 sites (actually, an arbitrary position also works). Concentric waves are automatically emitted from the pacemaker at $t = 450$ t.u., see Fig. 5b. The target waves are stable, and gradually invade into the region where spiral turbulence previously dominate, see Fig. 5c. Finally, after $t = 1500$ t.u., the whole system is dominated by one large target wave and the control is achieved, as shown in Fig. 5d.

As proved by previous experiments [34–36] as well as numerical simulations of inhomogeneous CGLE [37], introducing the pacemaker changes the local frequency of the bulk oscillation (ω_0) [38]. The frequency change in the local area should be large enough to show the inhomogeneity, which is necessary to create a target wave. In our simulations, we find that the difference of c should be larger than 0.3. As a result, a target wave with the same frequency as the pacemaker (ω_T) is generated. Inside the introduced small area, the system is in the state of homogeneous oscillation with frequency $\omega_T = c_I$ [39], this determines the frequency of the target wave outside of the small area, where the dispersion relation holds (see eq. 4). As a result, we have $c_I = c + (b - c)k^2$, which gives the wave number k of the target wave:

$$k = \sqrt{(c - \omega_T)/(c - b)} = \sqrt{(c - c_I)/(c - b)} \tag{5}$$

According to eq. 5, with the fixed b and c, the value of k will decrease with the increase of the value of ω. Thus, it is possible to drive the wave number of the traveling wave from an absolutely unstable region to a convective unstable region (see Fig. 4) by increasing the frequency of a traveling wave. This region is displayed in $\omega - c$ or $c_I - c$ plane in Fig. 6, where the solid line corresponds to the onset of absolute instability for plane waves, which determines the minimum and the maximum of ω_T. The vertical dashed line ($c = 0.8$) is the onset of absolute instability for spiral waves; thus, a target wave is stable, but a spiral wave is unstable in the area defined by the dashed line and the solid line in Fig. 6. The dotted line in the middle represents the existence condition for target wave, beyond which target waves cannot be automatically generated by introducing a pacemaker in a local region.

In addition to the fact that the target wave is stable, to achieve control of spatiotemporal chaos, the target wave should be able to develop, which means that the domain walls between target wave and spiral turbulence should move outward, thus, the target wave eventually should dominate the whole system. In the parameter space of CGLE that we are now interested in, i.e., $b = -1.4$, $c > 0$, $c_I > 0$, $|\omega_T| < c = |\omega_0|$, the frequency of the bulk oscillation is larger than the asymptotic frequency of the wave. Thus, the movement of domain walls is a result of competition between antitarget waves and antispiral waves [39]. The request that the phase of the solution must be continuous across domain boundaries provides

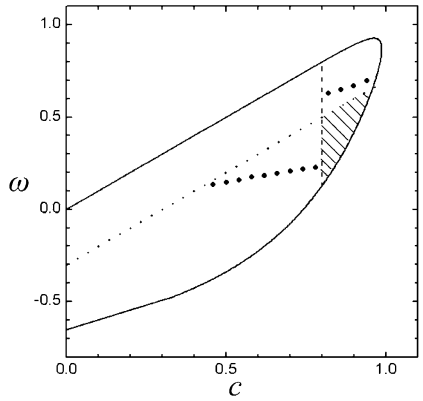

Fig. 6 Phase diagram in the ω-c plane. The solid line and dashed line show the onset of absolute instability for plane waves and for spiral waves, respectively. The dotted line in the middle represents the existence condition for target wave $c_I \leq c - 0.3$. The black dots show the change of spiral wave frequency as a function of c. A sharp increase occurs at the onset of spiral turbulence. The hatched area is the region where the control can be achieved.

an equation for the velocity of the domain walls [40], which states that, for the case of $b < c$, as we have, the pattern with the lowest frequency will dominate. Spiral wave solutions in an absolutely unstable parameter region can be regarded as little spiral seeds with very short correlation length. The black dots in Fig. 6 show the frequency of spiral wave solutions ω as a function of c. A sharp frequency increase at the onset of spiral turbulence is observed. To have advantages of target waves over the spiral turbulence, ω_T or c_I must be smaller than the corresponding frequency of spiral wave solutions. As a result, the hatched area in Fig. 6 is the region where the spiral turbulence can be controlled by introducing a pacemaker and generating a target wave in the system. The value of c_I can continuously change inside the region. Simulation results with different c_I are consistent with this analysis.

The major advantage of our method of controlling defect-mediated turbulence or spiral turbulence in the oscillation medium is that it is simple, convenient, and highly efficient. There is no need to trace or lock a certain spiral defect [41]. We only need to introduce a spatially localized pacemaker at an arbitrary position of the system. The high efficiency is also attractive. The change of the parameter value of 5×5 sites brings the change of dynamics behavior of the whole 512×512 region.

Furthermore, we emphasize that the control scheme can be readily applied to a reaction–diffusion system. Notice that for a reaction–diffusion system, the CGLE describes the amplitude equation near the onset of supercritical Hopf bifurcation, inserting eq. 3 into eq. 1, one has: $u - u_0 \propto F(r) \exp\{i[\sigma\theta + \psi(r)] + (\omega_H T/t - \omega)t\} + c.c.$ Often (not always), we have $\omega_H T/t >> \omega$. So that in a reaction–diffusion system, we will observe a competition between target waves and spiral waves which both propagate outward, and the pattern with the highest frequency ($\omega_H T/t - \omega$) will dominate.

DOPPLER INSTABILITY

The Doppler instability occurs in excitable systems. Its mechanisms rise from a Hopf bifurcation contributing to the spiral core, which makes the spiral meandering. Owing to the Doppler effect, with sufficiently large meandering, defects can be generated when two adjacent wave fronts near the core are too close, so that the local wavelength is beyond the critical value allowed by the dispersion relation.

In the experiment, we use the concentration of the malonic acid as the control parameter with the others fixed. At high malonic acid concentration, we observe a periodic (simple) rotating spiral, as shown in Fig. 7d. The tip of the spiral follows a small circle, as indicated in Fig. 7a. When the malonic acid concentration is decreased across a critical value, the system undergoes a transition from simple rotating spirals to meandering spirals [29,42–44], and the time dependence of the concentrations at any

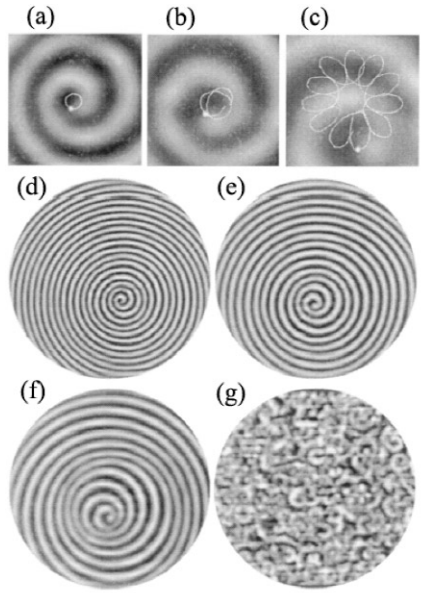

Fig. 7 Images illustrating the transition from a regular spiral to meandering spirals and to spiral turbulence as the malonic acid concentration is decreased. (a–c) Enlargements of the central part of (d–f). The white lines in (a–c) show the orbit of the spiral tip, and the white dots mark the location of the spiral tips in the background. Malonic acid concentrations: (a), (d) 0.40 M, simple spiral; (b), (e) 0.30 M, onset of meandering spiral; (c), (f) 0.13 M, large meandering spiral; (d), 0.10 M, spiral turbulence. Other control parameters were kept fixed: $[NaBrO_3]_{A(B)} = 0.4$ M; $[KBr]_A = 30$ mM; $[H_2SO_4]_B = 0.4$ M; $[Ferroin]_B = 0.5$ mM; residence time in each reservoir, 11 min; temperature 25 ± 0.5 °C. The region shown in (a–c) is 7.5×7.5 mm^2; (d–g) 19.5 mm in diameter.

point in the reaction–diffusion medium changes from periodic to quasi-periodic. Two types of meandering motion have been observed in previous work: hypocycloid (outward flower petals) and epicycloid (inward flower petals) [29,42–45]. Under our experimental conditions, the tip follows a hypocycloid trace, as shown in Fig. 7b. The orbit is similar to an earth–moon pattern where the primary cycle (moon) orbits the secondary cycle (earth) in one direction and rotates about its center in the opposite direction [29]. As we decrease the malonic acid concentration in the meandering regime, the diameter of the secondary circle increases and the petals of spiral tip orbit grow. This large meandering motion is shown in Fig. 7c. As a consequence of the Doppler effect, spiral waves in front of the spiral tip are compressed and those behind the spiral tip are dilated, as shown in Fig. 7f. The local oscillation period of the meandering spirals is found to vary regularly in a range between a minimum and a maximum value. The size of the petals of the spiral tip orbit increases continuously as the malonic acid concentration is decreased, so that the Doppler effect on the spiral waves becomes more and more pronounced. When the control parameter passes a second critical value (0.12 M), the system undergoes another transition characterized by the Doppler instability: spiral waves near the spiral center break and the system spontaneously generates new spiral tips (defects). This process continues until the whole system is filled with defects. Thus, the asymptotic state of the system is a state of spatiotemporal turbulence, as shown in Fig. 7g.

Figure 8 illustrates the spiral-breaking process. As the spiral tip moves toward its adjacent wave, it breaks the wave and generates a pair of defects, as shown in Figs. 8a and 8b. The newly generated defects drift apart and self-organize into new spiral rotors. The daughter spirals meander in the same way as the mother; hence, the daughters similarly break and generate their own daughters, as shown in Fig. 8c. The number of spiral tips continuously increases (Fig. 8d) until the system is saturated with spiral defects (Fig. 7g).

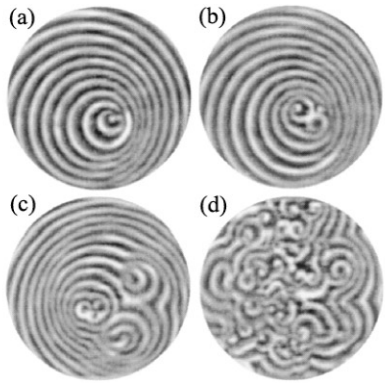

Fig. 8 The development of spiral turbulence as a single spiral undergoes a Doppler instability: (a) $t = 0$, a pair of defects is just generated; (b) $t = 100$ s, new defects self-organize into spirals; (c) $t = 400$ s, daughter spirals give birth to granddaughter spirals; (d) $t = 2000$ s, spiral turbulence. The control parameters are the same as in Fig. 7 (with 0.10 M malonic acid concentration). The region shown is 19.5 mm in diameter.

The observed phenomena can be well explained by an instability mechanism which was proposed by Bär et al. [10]. The argument is the following: The dispersion relation that relates the speed to the period of the traveling waves governs the behavior of spiral waves in an excitable medium. The speed of the waves depends on how well the local system recovers to its quiescent state after being excited; hence, it is an increasing function of the period of waves [17]. There exists a minimum period $p_{\min}$ below which the system cannot recover to its excitable state, and traveling waves will cease to exist [17,18]. Generally, the period of a regular spiral waves is a little larger than the minimum period, thus, spiral waves are stable. However, when a spiral tip meanders, the local period of its waves varies because of the Doppler effect. For sufficiently large meandering, the local period of spiral waves (p_0) becomes less than $p_{\min}$, rendering the local chemical waves unstable, and defects are spontaneously created. Figures 8a–8b clearly demonstrate this process.

CONTROL OF DOPPLER INSTABILITY

If we can successfully prevent the spiral tip from meandering, we may avoid the Doppler instability. In this section, we investigate the attractive effect of spiral tip by a small area with local diffusion coefficient inhomogeneity in a spatially extended two-variable FitzHugh–Nagumo model [46]. The normal FitzHugh–Nagumo model has the form:

$$\frac{du}{dt} = (a-u)(u-1)u - v + D_u \nabla^2 u$$

$$\frac{dv}{dt} = \varepsilon(bu - v) + D_v \nabla^2 v$$

where u and v are dimensionless excitable variable and recovery variable respectively; D_u and D_v are diffusion coefficients of the two variables. When $0 < a < 1$, $b \geq 0$, $D_v << D_u$, $\varepsilon << 1$, the equation describes an excitable medium. We set control parameters as follows: $a = 0.1$, $b = 1.0$, $\varepsilon = 0.005$, $D_u = 0.33$, $D_v = 0$, and simulate the model on a 256×256 grid of spatial points (space unit $h = 1$) with no-flux boundary condition. We create a spiral wave using the vertical gradient distribution in the initial condition. In the asymptotic state, the spiral tip follows a hypocycloid trajectory, showing a typical sign of meandering state [29] (see Fig. 9a).

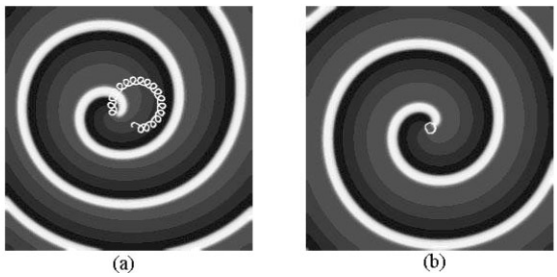

Fig. 9 (a) Spiral wave and its tip's motion in the homogenous media. The white curve is the trajectory of the spiral tip. (b) Spiral wave and its tip's motion in the media with a 10 × 10 grid area of inhomogeneity of diffusion coefficient.

Then we increase the diffusion coefficient in a small circular region Ω by D times. If we use D_u^{Ω} to denote the diffusion coefficient in region Ω, and use D_u^0 for the region outside of Ω, we have $D_u^{\Omega} = D \cdot D_u^0$. We find that the spiral tip can be attracted and travels around the region Ω when D is large enough and $R > R_0$ (R is the radius of Ω; R_0 is the core radius of spiral when $D_u^0 = D_u^{\Omega}$). At a given R, we can define two values D_1 and D_2: When $D < D_1$, the tip cannot be trapped; when $D > D_2$, the tip can be trapped for a long enough period. A temporal attraction occurs when $D_1 < D < D_2$; in this case, the tip can be trapped for a short period and then escapes; the trapped time increases with D. Defining D_c as the mean value of D_1 and D_2, the plot of D_c with different R is shown in the Fig. 10.

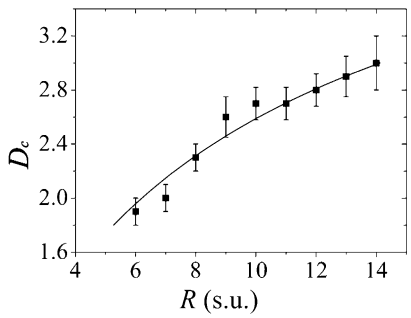

Fig. 10 The critical diffusion coefficient D_c as a function of R, where the line is the best fitting with eq. 6. The error bars are estimated using D_1 and D_2.

With the relation between the spiral core radius and the diffusion coefficient, the mechanism of the spiral tip attraction can be well understood. According to the analysis of the spiral tip dynamics given by Hakim and Karma [47], for a simple rotation spiral in an excitable medium, the core radius R as a function of diffusion coefficient can be written as:

$$R = \frac{D_u}{c_0}\left(\frac{bK}{B_c - \dfrac{2D_u}{W}}\right)^{3/2} \tag{6}$$

where D_u is the diffusion coefficient of the activator (u); c_0 is the speed of plane wave; b, K, and B_c are all constants. W is the constant width of the excited region. In our simulation, we assume that at the boundary of Ω there exists a "virtual" gradient region of D_u, which links the outside and inside regions. For a given R of the region $\Omega[R > R_0 = R(D_u^0)]$, the "trapped" motion of the spiral tip requires a spe-

cific value of D_u, satisfying eq. 6. When $D_u < D_u^{\Omega}$, the spiral tip will enter the gradient region where the system can find the required D_u, so that the spiral tip will rotate around the gradient area at the boundary of Ω; on the other hand, when $D_u > D_u^{\Omega}$, the "trapped" motion can not be sustained by the central region. From this argument, at critical point, we will have $D_u(R) = D_u^{\Omega} = D_c \cdot D_u^0$. As shown in Fig. 10, our simulation results are consistent with this analysis within the range of error.

By applying the eikonal equation, which determines the relation between the curvature of a traveling wave front and its speed in an excitable medium, and the Luther relation, which describes the relation between the speed of chemical waves and the diffusion coefficient of activator [48], we prove the "trapped" state of spiral tip motion is a stable state. The eikonal equation is: $N = C - D_u \cdot \kappa$, where N is the normal wave speed, κ is the local curvature of the wave front; the Luther equation is: $C = \alpha \cdot \sqrt{D_u}$, where α is a constant. Inserting the Luther equation into the eikonal relation, we have:

$$N = \alpha\sqrt{D_u} - D_u\kappa \tag{7}$$

Taking the partial derivative of R in eq. 7, we get:

$$\frac{\partial N}{\partial R} = \left[\frac{1}{2}\alpha\left(D_u\right)^{-1/2} - \kappa\right]\frac{\partial D_u}{\partial R} \tag{8}$$

At the spiral tip, we have $N = 0$, so that:

$$\left.\frac{\partial N}{\partial R}\right|_{\text{tip}} = -\frac{1}{2}\kappa_{\text{tip}}\frac{\partial D_u}{\partial R} \tag{9}$$

In our system, assuming a continuous change of D_u at the boundary of region Ω, we have $\partial D_u/\partial R < 0$. Thus, eq. 9 indicates that $\partial N/\partial R_{\text{tip}} > 0$. That means, if we introduce a small deviation from the "trapped" motion of the spiral tip, the system will return to the "trapped" state spontaneously, because we have $N < 0$ inside the region Ω, and $N > 0$ outside the region Ω ($\hat{n}$ points to the center of Ω region). Thus, the stability of the trapped state of spiral tip is proved.

We should note that there are other situations where the tip of spiral waves can be trapped in a given area. For example, Lázár et al. reported that self-sustained chemical waves can rotate around a central obstacle in an annular 2D excitable system, and the wave fronts in the case of an annular excitable region are purely involutes of the central obstacle in the asymptotic state [49]. Obviously, this phenomenon is beyond our analysis. More work should be done to fully understand the attractive effect of local inhomogeneities in an excitable reaction–diffusion system.

CONCLUSION

In conclusion, we have studied the two spiral instabilities, long-wavelength instability and Doppler instability, which have been observed in the BZ reaction–diffusion system. These two kinds of instability mechanisms of spiral waves represent typical ways from ordered spiral waves to defect-mediated turbulence in 2D reaction–diffusion systems. To achieve control of the two instabilities, we propose two pertinent strategies, respectively.

The two instabilities are both on the basis of the 2D structure. However, the 3D effects inevitably exist in the system. There are multiple chemical gradients existing across the reaction medium, which can play a crucial role under some conditions. Winfree discusses the effect of a non-negligible thickness of a reaction medium [50]. It turns out that if the thickness of the medium is larger than the diameter of the rotor, the rotor becomes 3D. Such a rotor may spontaneously generate defects unless confined to a layer thinner than about a rotor diameter. The 3D structure can surely change the dynamics of the system, such as the dispersion relation and spiral stabilities. There are abundant phenomena con-

cerned with 3D effects. A large-scale, 3D investigation is in hand, including simulation and experiment work. And recently, some control methods for 3D instability are proposed.

ACKNOWLEDGMENTS

This work is supported by grants from the Chinese Natural Science Foundation and Department of Science and Technology in China.

REFERENCES

1. J. M. Dadivenko, A. V. Pertsov, R. Salomonsz, W. Baxter, J. Jalife. *Nature* **355**, 349 (1992).
2. A. T. Winfree. *Science* **266**, 1003 (1994).
3. L. Glass. *Phys. Today* **8**, 40 (1996).
4. P. Coullet, L. Gil, J. Lega. *Phys. Rev. Lett.* **62**, 1619 (1989).
5. J.-P. Eckmann and I. Procaccia. *Phys. Rev. Lett.* **66**, 891 (1991).
6. G. Hub, P. Alstrøm, T. Bohr. *Phys. Rev. Lett.* **69**, 2380 (1992).
7. I. Aranson, L. Kramer, A. Weber. *Phys. Rev. Lett.* **72**, 2316 (1994).
8. M. Ipsen and P. G. Sørensen. *Phys. Rev. Lett.* **84** , 2389(2000).
9. Q. Ouyang and J.-M. Flesselles. *Nature* **379**, 143 (1996).
10. A. Belmonte, J.-M. Flesselles, Q. Ouyang. *Europhys. Lett.* **35**, 665 (1996).
11. J.-S. Park and K. J. Lee. *Phys. Rev. Lett.* **83**, 5393 (1999).
12. Q. Ouyang, H. L. Swinney, G. Li. *Phys. Rev. Lett.* **84**, 1047 (2000).
13. M. Bär, M. Hildebrand, M. Eiswirth, M. Falcke, H. Engel, M. Neufeld. *Chaos* **4**, 499 (1994).
14. M. Bär and M. Or-Guil. *Phys. Rev. Lett.* **82**, 1160 (1999).
15. A. Goryachev, H. Chaté, R. Kapral. *Phys. Rev. Lett.* **80**, 873 (1998).
16. A. Goryachev, H. Chaté, R. Kapral. *Phys. Rev. Lett.* **83**, 1878 (1999).
17. J. P. Kneener and J. J. Tyson. *Physica D* **21**, 307 (1986).
18. J. D. Dockey, J. P. Kneener, J. J. Tyson. *Physica D* **30**, 177 (1988).
19. K. I. Agladze and P. DeKepper. *J. Phys. Chem.* **96**, 5239 (1992).
20. S. Nettesheim, A. von Oertzen, H. H. Rotermund, G. Ertl. *J. Chem. Phys.* **98**, 9977 (1993).
21. X. N. Wang, Y. Lu, M. X. Jiang, Q. Ouyang. *Phys. Rev. E* **69**, 056223 (2004).
22. I. S. Aranson and L. Kramer. *Rev. Mod. Phys.* **74**, 99 (2002).
23. I. Aranson, H. Levine, L. Tsimring. *Phys. Rev. Lett.* **72**, 2561 (1994).
24. H. Zhang, B. Hu, G. Hu, Q. Ouyang, J. Kurths. *Phys. Rev. E* **66**, 046303 (2002).
25. M. X. Jiang, X. N. Wang, Q. Ouyang, H. Zhang. *Phys. Rev. E* **69**, 056202 (2004).
26. Q. Ouyang and H. L. Swinney. *Chaos* **1**, 411 (1991).
27. J. Pearson and W. Bruno. *Chaos* **2**, 513 (1992).
28. V. Duffiet and J. Boissonade. *Phys. Rev. E* **53**, 4883 (1996).
29. G. Li, Q. Ouyang, V. Petrov, H. L. Swinney. *Phys. Rev. Lett.* **77**, 2105 (1996).
30. A. L. Belmonte, Q. Ouyang, J. M. Flesselles. *J. Phys. II France* **7**, 1425 (1997).
31. B. Janiaud et al. *Physica D* **55**, 269 (1992).
32. I. S. Aranson, L. Aranson, L. Kramer, A. Weber. *Phys. Rev. A* **46**, R2992 (1992).
33. L. Kramer, F. Hynne, P. G. Sørenson, D. Walgraef. *Chaos* **4**, 443 (1994).
34. A. T. Winfree. *Theor. Exp. Chem.* **4**, 1 (1978).
35. A. E. Bugrim, M. Dolnik, A. M. Zhabotinsky, I. R. Epstein. *J. Phys. Chem.* **100**, 19017 (1996).
36. K. J. Lee, E. C. Cox, R. E. Goldstein. *Phys. Rev. Lett.* **76**, 1174 (1996).
37. M. Hendrey, K. Nam, P. Guzdar, E. Ott. *Phys. Rev. E* **62**, 7627 (2000).
38. V. K. Vanag and I. R. Epstein. *Science* **294**, 835 (2001).
39. Y. Gong and D. J. Christini. *Phys. Rev. Lett.* **90**, 088302 (2003).
40. K. Nam, E. Ott, M. Gabbay, P. Guzdar. *Physica D* **118**, 69 (1998).

41. K. Wang, X. M. Mao, Q. Ouyang. *Chin. Phys. Lett.* **18**, 834 (2001).
42. D. Barkley, M. Kness, L. S. Tuckerman. *Phys. Rev. Lett.* **42**, 2489 (1990).
43. W. Jahnke and A. T. Winfree. *Intl. J. Bif. Chaos* **1**, 445 (1991).
44. V. Hakim and A. Karma. *Phys. Rev. Lett.* **79**, 665 (1997).
45. V. Zykov. *Biophysics* **31**, 940 (1986).
46. R. A. FitzHugh. *Biophys. J.* **1**, 445 (1966).
47. V. Hakim and A. Karma. *Phys. Rev. E* **60**, 5073 (1999).
48. R. Arnold, K. Showalter, J. J. Tyson. *J. Chem. Educ.* **64**, 740 (1987).
49. A. Lázár, Z. Nosztizius, H. Farkas. *Chaos* **5**, 443 (1995).
50. A. T. Winfree. *Nature* **371**, 233 (1994).